Title

Single pulse protoacoustic range verification using a clinical synchrocyclotron

Journal

Physics in Medicine and Biology, 68(4)

ISSN

0031-9155

Authors

Caron, Joseph

Gonzalez, Gilberto

Pandey, Prabodh Kumar

et al.

Publication Date

2023-02-21

DOI

10.1088/1361-6560/acb2ae

Peer reviewed

HHS Public Access

Author manuscript

Phys Med Biol. Author manuscript; available in PMC 2023 October 11.

Published in final edited form as:

Phys Med Biol. ; 68(4): . doi:10.1088/1361-6560/acb2ae.

Single pulse protoacoustic range verification using a clinical synchrocyclotron

Joseph Caron[1], **Gilberto Gonzalez**[1], **Prabodh Kumar Pandey**[2], **Siqi Wang**[3], **Kiana Prather**[4], **Salahuddin Ahmad**[1], **Liangzhong Xiang**[2,3,5,*], **Yong Chen**[1,*]

[1]Department of Radiation Oncology, University of Oklahoma Health Sciences Center, Oklahoma City, OK, 73104, United States of America

[2]Department of Radiological Sciences, University of California at Irvine, Irvine, CA 92697, United States of America

[3]The Department of Biomedical Engineering, University of California, Irvine, CA 92617, United States of America

[4]University of Oklahoma College of Medicine, Oklahoma City, OK, 73104, United States of America

[5]Beckman Laser Institute & Medical Clinic, University of California, Irvine, Irvine, CA 92612, United States of America

Abstract

Objective.—Proton therapy as the next generation radiation-based cancer therapy offers dominant advantages over conventional radiation therapy due to the utilization of the Bragg peak; however, range uncertainty in beam delivery substantially mitigates the advantages of proton therapy. This work reports using protoacoustic measurements to determine the location of proton Bragg peak deposition within a water phantom in real time during beam delivery.

Approach.—In protoacoustics, proton beams have a definitive range, depositing a majority of the dose at the Bragg peak; this dose is then converted to heat. The resulting thermoelastic expansion generates a 3D acoustic wave, which can be detected by acoustic detectors to localize the Bragg peak.

Main results.—Protoacoustic measurements were performed with a synchrocyclotron proton machine over the exhaustive energy range from 45.5 to 227.15 MeV in clinic. It was found that the amplitude of the acoustic waves is proportional to proton dose deposition, and therefore encodes dosimetric information. With the guidance of protoacoustics, each individual proton beam (7 pC/pulse) can be directly visualized with sub-millimeter (<0.7 mm) resolution using single beam pulse for the first time.

Significance.—The ability to localize the Bragg peak in real-time and obtain acoustic signals proportional to dose within tumors could enable precision proton therapy and hope to progress towards *in vivo* measurements.

*Authors to whom any correspondence should be addressed. yong-chen@ouhsc.edu and liangzhx@hs.uci.edu.

Supplementary material for this article is available online

Keywords

proton therapy; range verification; protoacoustics; ionoacoustics

1. Introduction

Radiation therapy is a highly effective tool for cancer treatment since it kills tumor cells or slows their growth by damaging their DNA (Hall and Giaccia 2019). However, while radiation therapy targets the tumor volume, it can also damage the surrounding normal tissue. Thus, conventional radiation therapy has not been considered as precision medicine since the damage to normal cells can cause harmful side effects (Freedman et al 2006, Chitapanarux et al 2019, Droge et al 2021). Protons offer dominant advantages over photons for radiation therapy due to its unique depth-dose characteristics which can be observed from their single beamlets (Paganetti 2019) (called Bragg peak-figure 1(a)). An individual photon beamlet delivers its maximum energy shortly after passing through the skin, whereas the proton beamlet has a distinct peak of energy which may allow dose escalation to the tumor target volume while sparing the tumor-neighboring susceptible organs at risk. This characteristic of proton dose fall-off has the potential to reduce treatment toxicity (Brown et al 2013, Harrabi et al 2016). Conventional radiation therapy uses a combination of several photon beamlets to ensure high tumor dose conformity and reduce surface dose, whereas proton therapy requires significantly less beamlets.

While proton therapy potentially allows better dose conformity due to the Bragg peak and utilization of pencil beam scanning with adaptive apertures, shown in figure 2(a), the full potential of the Bragg peak is yet to be exploited because of the ‘range uncertainty’ (Paganetti 2012, Jones et al 2016). Multiple sources of range uncertainty include the conversion from the computed tomography (CT) value to stopping power ratio (Schaffner and Pedroni 1998, Taasti et al 2018), anatomical changes of the patient, and organ motion (Lambert et al 2005, Su et al 2019). Range uncertainty can have consequences on several aspects of a treatment, including target coverage, dose conformation, dose homogeneity, and critical organ doses (Lin et al 2008, Tryggestad et al 2020). This uncertainty remains during the actual dose delivery in proton therapy, thus calling for additional methods for *in vivo* assessment of the proton beam range or, ideally, dose delivery during treatment (Assmann et al 2015, Paganetti 2019). Four methods have been proposed so far, namely prompt gamma detection (PGD) (Tian et al 2021), positron emission tomography (PET) (Parodi et al 2007, Zhu and El Fakhri 2013), phase-change ultrasound contrast agents (Carlier et al 2020, Collado-Lara et al 2022) and protoacoustics (Jones et al 2015, Lehrack et al 2017, Hickling et al 2018). PGD and PET detect the gamma-ray arising from the proton-nuclei reactions along the beam path and can measure range with an accuracy within a few millimeters. However, PET still is not able to offer imaging in real-time (Cherry et al 2018). PGD can perform real-time measurements, but it possesses disadvantages such as the inability to correlate photon intensity to deposited dose, and the rather complex and expensive detectors required (Wroska 2020). Additional methods for proton range verification have been investigated such as phase-change ultrasound contrast agents which generates contrast from the vaporization of superheated nanodroplets (Collado-Lara et al

2022), while conventional protoacoustics benefits from the pressure waves released during thermoelastic expansions of pulsed proton energy depositions (Assmann et al 2015).

Experimental observation of acoustic waves induced by a proton beam from a patient were first reported in 1995 (Hayakawa et al 1995), and there has been renewed interest in this technique over the last few years due to upgraded proton machines and ultrasound detectors. Unlike PGD and PET, which require bulky and expensive gamma-ray detectors around patients, protoacoustic detection systems comprise of a single detector or an array of ultrasound detectors, which only require a small space and are more affordable. Recently, many studies have been conducted by our group (Ahmad et al 2015, Pratik Samant et al 2022) and other groups (Kellnberger et al 2016, Lehrack et al 2017, Patch et al 2021) to reduce the range uncertainty during proton therapy by exploiting protoacoustics. These experiments were performed using a linac (Sulak et al 1979), synchrotron (Hayakawa et al 1995), synchrocyclotron (Lehrack et al 2017) and isochronous cyclotron Jones et al 2015), all with encouraging results. Moreover, the protoacoustic image can be a perfectly co-registered overlay of the Bragg peak onto an ultrasound image (Patch et al 2021). These latest studies demonstrated the feasibility of using protoacoustic imaging as a viable range verification technique in a clinical radiotherapy environment. However, the real clinical application has been hampered by the weak protoacoustic signal (Lascaud et al 2021). In return, the dose sensitivity is low (>10 Gy), and more than 1000 averages were needed to obtain a reasonable signal-to-noise ratio for protoacoustic signals (Lehrack et al 2017), which renders the real-time localization of the Bragg peak during proton therapy virtually impossible.

In this paper, a strategy was developed to use high-precision range verification for proton therapy, enabled by a protoacoustic system shown in figure 2(b), which can: (1) monitor the position of the Bragg peak, and (2) quantify the radiation dose in tumor in real time. The feasibility of protoacoustic detection as an *in vivo* method for measuring the range of proton dose depositions during patient treatments was investigated by measuring proton dose depositions across the entire energy range of a clinical proton system utilized in patient treatments with single pulse signal acquisitions from a transducer. With generated protoacoustic signals, the utilization of a trigger signal from the proton system shown in figure 2(c), and the application of a Savitzky–Golay digital filter, an appreciable signal-to-noise ratio (SNR) is obtained for single pulse signals (figure 2(d)) that demonstrates promise for clinical implementation.

2. Material and methods

2.1. Time-of-flight measurement of protoacoustics

In pulsed radiation therapy, a pressure wave is induced in the medium due to the deposited dose, or deposited energy, causing microscopic thermal expansion if the excitation pulse is small enough (on the order of microseconds). This generation and propagation of the acoustic signal (in this case, protoacoustic) under the assumptions of thermal confinement and negligible acoustic attenuation can be expressed as:

$$\left(\nabla^2 - \frac{1}{c^2}\frac{\partial}{\partial t^2}\right)p\left(\vec{r},t\right) = -\frac{\beta}{C_p}\frac{\partial H\left(\vec{r},t\right)}{\partial t}, \quad (1)$$

where $p\left(\vec{r},t\right)$ denotes the acoustic pressure at location $\vec{r}$ and time t, c is the speed of sound, β is the thermal expansion coefficient, C_p is the target's heat capacity at a constant pressure, and $H\left(\vec{r},t\right)$ is the heating function which can be decomposed into separate spatial and temporal functions as $H\left(\vec{r},t\right) = E\left(\vec{r}\right)F(t)$, with $E\left(\vec{r}\right)$ and $F(t)$ being the proton energy deposition in the tissue and temporal proton pulse.

The solution to equation (1) due to delta pulse excitation ($F(t) \approx \delta(t)$) is given as:

$$p_G\left(\vec{r},t\right) = \frac{\beta}{4\pi C_p}\frac{\partial}{\partial t}\left(\frac{1}{ct}\int_{S\left(\vec{r},t\right)} H(\vec{r}')dS'(t)\right);\ |\vec{r} - \vec{r}'| = vt, \quad (2)$$

where $S'(t)$ denotes a time-dependent spherical surface centered at the detector location $\vec{r}$ such that $|\vec{r} - \vec{r}'| = ct$. The protoacoustic signal generated due to a proton pulse function $F(t)$ will be:

$$p\left(\vec{r},t\right) = F(t) * p_G\left(\vec{r},t\right). \quad (3)$$

The finite temporal width of the proton pulse leads to the widening of the protoacoustic signals. In protoacoustics, protons cause an abrupt temperature rise at the location of deposition. Due to the unique nature of the Brag peak, protons that are deposited in the pre-Bragg peak region will emit a cylindrical pressure wave from the axis of deposition whereas the protons deposited in the Bragg peak region emit a spherical pressure wave that mainly propagates distal to the Bragg peak along the axis of deposition (Assmann et al 2015). These waves are denoted as the α wave and the γ wave, respectively (Jones et al 2016,2018). The wave of interest in this work is the γ wave. Assuming negligible noise contribution, the time-of-flight calculation for the γ wave when the detector is placed distal to the Bragg peak on the beam axis can be determined by:

$$\tau = \frac{1}{c}, \quad (4)$$

where τ is the arrival time, c is the speed of sound in the medium, and l is the on-axis distance of the detector surface from the Bragg peak. The ideal arrival time can be meaningfully linked back to the Bragg peak location. The arrival times are measured and compared from both the simulation and experiment.

2.2. Range verification experimental setup

Proton induced acoustic range measurements were performed with a proton synchrocyclotron (Mevion S250i Hyperscan) at energies ranging from 45.5 to 227.15 MeV,

which correlates to D_{90} depth distances of 1.9 cm to 32.2 cm. The D_{90} depth is defined as the depth at which 90% of the distal portion of the Bragg peak occurs. The gantry of the system was positioned to deliver a horizontal beam into a water tank with an entrance window on the side to reduce attenuation of the beam. The extension was completely retracted and the isocenter of the system was set to be 15 cm from the entrance window of the tank, leaving an air gap of 18.6 cm. Since the central frequency of the induced signal was measured to be around 30 kHz in water with a proton dose deposition, a low-frequency 0.5 MHz transducer (Olympus V389-SU) was used. This transducer was positioned in the tank along the beam axis, with the surface of the transducer at a distance of approximately 34 cm from the entrance window of the tank. The transducer was placed approximately 10 cm from the water surface, which is low enough to reduce reflections. The transducer was then connected to a two-stage amplification system placed in a borated-polyethylene shielding box. The first stage preamplifier (Olympus 5660B Preamp) had 40 dB amplification and the second stage preamplifier (SRS SR560 Low-Noise Preamplifier) had a low noise amplification of 60 dB, with a set 6 dB bandwidth of 3–100 kHz. This bandwidth was selected based on the frequency of the signal collected in order to effectively eliminate noise that occurs outside this bandwidth. This resulted in a maximum signal amplification of 100 dB. The signal was then connected to a dispatch board and sent outside the treatment room to the console patch panel to be connected and viewed on a digital oscilloscope (RigolDS1202). Data on the oscilloscope was stored with a sampling time of 500 ns. A charge deposition of 1 pC corresponds to 0.0685 MU, therefore the smallest deposition of charge seen in patient treatments is approximately 4 pC. With this in mind, various datasets were gathered with charges-per-pulse ranging from 3 to 7 pC/pulse in order to ensure that the charge-per-pulse utilized was on the order of the smallest depositions seen in patient treatments. The diagram of the experimental setup and signal pathway can be found in the supplementary material.

2.3. Dosimetric verification experimental setup

A similar setup as in the range verification experiment was used. Single pulse signals were acquired with a charge-per-pulse deposition that varied from 2 to 9 pC/pulse. A beam energy of 162.78 MeV, which correlates to approximately 18 cm, was delivered with the transducer placed at a depth distance of 28 cm. The range variations along with the peak-to-peak voltage of the various signals were measured and analyzed.

2.4. K-wave simulation

To have an objective and consistent correlation point in the analysis of the range verification signals, dose induced acoustic signals were simulated in the k-wave toolbox. This point of analysis is essential in correlating the percent-maximum in the protoacoustic signal to the D_{90} depth distance of the proton beam. Three-dimensional depth-dose data was obtained from commissioning of the proton system and was used to simulate the dose deposition for various beam energies. The dose files used had energies ranging from 200 to 40 MeV. The resolution of the medium was chosen based on the resolution of the dose files, which varied from 0.5 to 0.1 mm. The sampling time and total collection time for the various simulation parameters were 0.1 μs and 25 μs, respectively. For a transducer in the medium that is placed 2 cm from the D_{90} deposition and centered on the beam axis, the total collection time used

is sufficient for total signal collection. The speed of sound used for the medium was 1498 m s^{-1} to represent that of distilled water. It was important to run simulations with various beam energies since the spot size increases with increasing energy, which affects the signal compression on the time axis. Therefore, this would affect the correlation point since a percent-maximum method was utilized. The protoacoustic signals produced from the k-wave simulation were convolved with a square wave signal to simulate a pulse width of 4.0 μs.

In the simulation, the correlation point was calculated for each energy based on the speed of sound in the homogenous medium and the distance between the D_{90} range of the beam and the placed position of the transducer in the simulation space. The percent-maximum of the induced signal at which the correlation point occurs was calculated for each beam energy simulated and then applied to the experimental data. The percent-maximum of the induced signal at which the correlation point occurs for each energy and pulse-width type is shown in table 1.

2.5. Signal analysis

With the signals acquired in data collection, the time between the beam current trigger of the proton system and the percent maximum of the rising edge of the first peak of the protoacoustic signal was used to calculate the distance between the transducer and the D_{90} range of the beam. This distance then infers the range of the proton dose deposition. To collect the protoacoustic signals, a trigger signal is required, which is usually considered to be the rising edge of the beam pulse signal. For practicality, we made use of the machine beam current which was available from outside the bunker at the treatment console. This machine beam current signal, however, comes with a considerable delay, which was corrected by using a fast-response scintillator. The delay between the beam current trigger and the scintillator was measured and incorporated into the calculations. A typical ionoacoustic signal can be seen in figure 2(c), where the signal induced by the proton beam occurs approximately at 50 μs and the reflection signal from the wall of the tank occurs at approximately 350 μs. This signal was obtained with a 3 pC deposition and 1024 signal averaging on the oscilloscope.

Single pulse acquisitions are necessary with the implementation of pencil beam scanning in proton therapy, where single spots may be deposited once per location in the treatment plan. The feasibility of single pulse acquisition was explored by quantifying the SNR of the protoacoustic signal. Various amounts of signal averaging were utilized in data collection, and it was observed that a decrease in averaging produced a decrease in SNR of the protoacoustic signal. The SNR was calculated to depreciate from approximately 30 dB at 32 signal averages to approximately 5 dB with single pulse acquisitions with the implementation of a Savitzky–Golay filter. Without this filter, the SNR of the signal was approximately −5 dB, concluding that digital filtering is crucial in acquisitions of single pulse signals of adequate SNR. Based on the three ranges of averaging that result in different levels of SNR, three amounts of averaging were chosen to investigate the amount of SNR needed for a specific level of accuracy: 1024 averages, 4 averages, and single-pulse acquisitions.

2.6. Range verification evaluation

In order to measure the Bragg peak localization for utilization in patient treatments, an experiment was designed and executed. Beam energies ranging from 45.5 to 227.15 MeV, in approximately 20 MeV increments, were delivered with various amounts of signal averaging. Five signals were acquired per beam depth used and the mean range depth of these signals was calculated. Three data sets were gathered to investigate the accuracy of this method with various charge-per-pulse depositions. With the smallest single deposition of charge in patient treatments being 4 pC, data sets contained 1024 average signals with 3 pC/pulse, 4 average signals with 4 pC/pulse, and single pulse signals with 7 pC/pulse. The energy-range relationship of the protoacoustic results were compared to that of the ionization depth-dose (IDD) of the proton system taken from commissioning, which utilizes an ion chamber.

3. Results

3.1. Range verification evaluation

Figure 3(a) shows the energy-range relationship of the proton system. Signals of 1024 averages, 4 averages, and single pulse are compared to the measured ionization depth dose (IDD) that signals of 1024 averages had all energies within approximately 0.5 mm of the ion chamber data (figure 3(b)). The standard error in these measurements were calculated to be approximately 0.1 mm. Some data points have a standard error of 0 mm, since the range depth was calculated to be the same for all five acquisitions for that energy. Signals of 4 averages were measured to be within approximately 1 mm of the ion chamber data (figure 3(c)). The standard error was calculated to have increased slightly with increasing distance from the transducer, with the maximum standard error of approximately 1.3 mm. Single-pulse signals were measured to be within 1 mm of the ion chamber data (figure 3(d)). The maximum standard error was calculated to be approximately 0.7 mm. At least 7 pC/pulse was necessary to obtain submillimeter results with single pulse due to substantial noise contributions.

The previous data with promising single pulse results was supported by further altering the range in 2 mm steps, which is the smallest alteration possible with the proton system. With a 2 mm shift in water corresponding to approximately 1.3 μs, and the sampling time of the signals being 0.5 μs, this shift is decipherable in the displayed signals with a separation of 1.5 μs (figure 4(a)). This experiment was performed using 3 pC/charge and beam energies of 186.05, 187.01, 187.94 MeV, with an approximate distance of 12 cm between Bragg peak and transducer surface.

For the single-pulse acquisitions, the mechanics of proton bunch delivery was slightly altered in the proton system to obtain the submillimeter results. These mechanics are in place for comprehensive patient safety and more accurate charge delivery in patient treatments since beam deliverance can vary by approximately 20%. Normally, the proton bunch is delivered in 4 packages with the first being around 80% of the total charge mentioned. The next three would be divided across the final 20% in the charge delivery. This created some inadequate results with single pulse acquisitions since it was uncertain which

package was being collected in signal acquisitions, resulting in various levels of signal amplitude. The settings were changed for the single-pulse acquisitions to have all 100% of the charge delivered in 1 package to have a more certain knowledge of the charge delivery.

The dependence of the range variations and signal voltage on the charge deposition was investigated by acquiring various charge-per-pulse depositions that varied from 2 to 9 pC/pulse from single pulse signals. A beam energy of 162.78 MeV, which correlates to approximately 18 cm, was delivered with the transducer placed at a depth distance of 28 cm. Five sets of signals were acquired per charge deposition. The detected range variations of the fixed-energy single pulse protoacoustic signals from the corresponding IDD were measured (figure 4(b)). All mean measurements for the various charge depositions were measured to be within approximately 1.3 mm of the IDD, with the higher depositions being more accurate. The largest standard deviation recorded was approximately 0.8 mm, resulting from a 3 pC deposition. A qualitative assessment shows that higher charge depositions are more robust, supplementing the range verification results.

3.2. Dosimetric verification

The peak-to-peak voltage of the various signals were also measured, and the mean and standard deviation were then calculated for each charge deposition set (figure 4(c)). The data was then fit with a linear curve and was calculated to have an R-squared value of 0.994, implying a good fit. This dosimetric data implies that there is a linear relationship between the charge delivered and the amplitude of the signal, meaning that there is a relative means of assessing the deposited dose in the medium by relating this to the deposited charge.

4. Discussion

The feasibility of protoacoustic detection of proton dose depositions for proton range verification within a water phantom was investigated by measuring acoustic waves from proton beams across the entire energy range of a clinical synchrocyclotron with single pulse signal acquisitions from a transducer. The energy-range relationship developed from the protoacoustic signals were compared to that of an ion chamber measuring the ionization depth-dose. With single pulse acquisitions having sub-millimeter range variations, protoacoustic detection could potentially progress into an *in vivo* method for measuring proton dose depositions with high precision during patient treatments. This method preserves advantages for clinical applications, being the potential for real-time acquisitions, high SNR, high spatial resolution, and simple, low-cost equipment.

Protoacoustic techniques could be implemented into the clinical workflow (figure 5). By placing the transducer with ultrasound gel applied, there can be a method for verification of patient set-up and positioning that does not involve ionizing radiation. This can be done with the transducer operating in a transmit and receive mode like a typical ultrasound procedure to acquire position knowledge of the target within the patient (Hickling et al 2018, Oraiqat et al 2020, Zhang 2020). Also, once the patient is positioned correcdy with the transducer in place, a low-dose spot scan can be delivered at various depths within the patient to acquire range information of the treatment plan. Multiple depth deliveries would benefit the treatment planning aspect with more accurate knowledge of stopping power within

the body. Since slightly more dose would be given for such a technique, a less thorough approach can be utilized where one depth is delivered for just beam range assurances. This ‘scout’ scan can be used for adaptive pre-planning purposes. For purposes during the treatment, protoacoustics could provide a method of real-time range and dosimetric verification using the techniques shown previously. This would allow for online adaptive treatment where adjustments could be made while the treatment plan is being delivered. For post-treatment applications, the results obtained by the transducer could be used to compare to the log-file generated by the proton system for adaptive post-planning purposes. The log-file is generated after each beam is delivered, containing the range and charge output for each spot deposition for patient quality assurance applications.

The proposed combination of protoacoustic detection alongside diagnostic ultrasound has some technical challenges, mainly due to the mismatch of operating frequencies. A recent study demonstrated a dual-mode system for *in vivo* x-ray acoustics and ultrasound. However, this system used a commercial probe with a frequency range of 1–4 MHz, which has low sensitivity for x-ray acoustic detection (<250 kHz), thus had to collect about 300 signal averages to compensate for the poor SNR and sensitivity. In the future, novel transducer technologies should consider operating over a wide frequency spectrum to capture XACT waves with sufficient SNR while maintaining the high-frequency components for anatomical imaging.

The protoacoustic signals are largely affected by the beam parameters (energy, spot size and distance to the detector). Nevertheless, our results using low charge (3 pC) single beam pulse show a highly-precise range resolution within 2 mm step-size, at a large distance to detector. This step-size is the smallest step the energy modulators our proton system can create. These signals have a clear separation of approximately 1.5 μs. With a speed of sound in water of 1498 m s^{-1}, this separation approximately corresponds to the 2 mm range adjustment. In the clinical environment, the dose per pulse maybe higher and the distances to a fixed transducer may be shorter, so we believe that acquisition settings could be standardized for each patient.

However, patient’s anatomic heterogeneities possess distinct acoustic properties such as acoustic attenuation or speed of sound which can affect the expected time of arrival of the protoacoustic signal as compared to a water phantom. Further research could perform simulation-guided protoacoustic acquisitions by considering the CT images where a segmentation process can be used to assign different sound velocities and material density to aid the simulation and obtain expected proton range. Thus, specific protoacoustic propagation models could be applied to account for each patient. A recent study has proposed a deep-learning approach for *in vivo* dosimetry while considering the CT volume for the acoustic simulation (Jiang et al 2022). The proposed convolutional neural network was trained on multiple patients and allowed to predict 3D pressure and dose maps.

Another future challenge for such implementation would pose issues from impedance mismatches at the surface interface in addition to within the phantom structure for differing materials representing bone and tissue. Another pathway would be for implementation of a two-dimensional transducer array for image reconstruction. This would present benefits for

real-time imaging and internal organ motion management, in addition to an unconventional method of proton radiography.

Supplementary Material

Refer to Web version on PubMed Central for supplementary material.

References

Ahmad M et al. 2015 Theoretical detection threshold of the proton-acoustic range verification technique Med. Phys 42 5735–44 [PubMed: 26429247]

Assmann W et al. 2015 Ionoacoustic characterization of the proton Bragg peak with submillimeter accuracy Med. Phys 42 567–74 [PubMed: 25652477]

Brown AP et al. 2013 Proton beam craniospinal irradiation reduces acute toxicity for adults with medulloblastoma Int. J. Radiat. Oncol. Biol. Phys 86 277–84 [PubMed: 23433794]

Carlier B et al. 2020 Proton range verification with ultrasound imaging using injectable radiation sensitive nanodroplets: a feasibility study Phys. Med. Biol 65 065013 [PubMed: 32045902]

Cherry SR et al. 2018 Total-body PET: maximizing sensitivity to create new opportunities for clinical research and patient care J. Nucl. Med 59 3–12 [PubMed: 28935835]

Chitapanarux I et al. 2019 Conventional versus hypofractionated postmastectomy radiotherapy: a report on long-term outcomes and late toxicity Radiat Oncol. 14 175 [PubMed: 31610801]

Collado-Lara G et al. 2022 Spatiotemporal distribution of nanodroplet vaporization in a proton beam using real-time ultrasound imaging for range verification Ultrasound Med. Biol 48 149–56 [PubMed: 34629191]

Droge LH et al. 2021 Conventional 3D conformal radiotherapy and volumetric modulated arc therapy for cervical cancer: comparison of clinical results with special consideration of the influence of patient- and treatment-related parameters Strahlenther Onkol. 197 520–7 [PubMed: 33938967]

Freedman GM et al. 2006 Intensity modulated radiation therapy (IMRT) decreases acute skin toxicity for women receiving radiation for breast cancer Am. J. Clin. Oncol 29 66–70 [PubMed: 16462506]

Hall EJ and Giaccia AJ 2019 Radiobiology for the Radiologist. Eighth edition (Philadelphia: Wolters Kluwer) vol. vii, p. 597

Harrabi SB et al. 2016 Dosimetric advantages of proton therapy over conventional radiotherapy with photons in young patients and adults with low-grade glioma Strahlenther Onkol. 192 759–69 [PubMed: 27363701]

Hayakawa YTJ, Arai N, Hosono K, Sato M, Wagai T, Tsuji H and Tsujii H 1995 Acoustic pulse generated in a patient during treatment by pulsed proton radiation beam. Radiat. Oncol. Investigations 3 42–5

Hickling S et al. 2018 Ionizing radiation-induced acoustics for radiotherapy and diagnostic radiology applications Med. Phys 45 e707–21 [PubMed: 29679491]

Jiang Z et al. 2022 3D *in vivo* dose verification in prostate proton therapy with deep learning-based proton-acoustic imaging Phys. Med. Biol 67 215012

Jones KC et al. 2015 Experimental observation of acoustic emissions generated by a pulsed proton beam from a hospital-based clinical cyclotron Med. Phys 42 7090–7 [PubMed: 26632062]

Jones KC et al. 2016 Acoustic time-of-flight for proton range verification in water Med. Phys 43 5213 [PubMed: 27587053]

Jones K et al. 2018 Acoustic-based proton range verification in heterogeneous tissue: simulation studies Phys. Med. Biol 63 025018 [PubMed: 29176057]

Kellnberger S et al. 2016 Ionoacoustic tomography of the proton Bragg peak in combination with ultrasound and optoacoustic imaging Sci. Rep 6 29305 [PubMed: 27384505]

Lambert J et al. 2005 Intrafractional motion during proton beam scanning Phys. Med. Biol 50 4853–62 [PubMed: 16204877]

Lascaud J et al. 2021 Enhancement of the ionoacoustic effect through ultrasound and photoacoustic contrast agents Sci. Rep 11

Lehrack S et al. 2017 Submillimeter ionoacoustic range determination for protons in water at a clinical synchrocyclotron Phys. Med. Biol 62 L20–30 [PubMed: 28742053]

Lin L et al. 2008 Dosimetric uncertainty in prostate cancer proton radiotherapy Med. Phys. 35 4800–7 [PubMed: 19070212]

Oraiqat I et al. 2020 An ionizing radiation acoustic imaging (iRAI) technique for real-time dosimetric measurements for FLASH radiotherapy Med. Phys 47 5090–101 [PubMed: 32592212]

Paganetti H 2012 Range uncertainties in proton therapy and the role of Monte Carlo simulations Phys. Med. Biol 57 R99–117 [PubMed: 22571913]

Paganetti H 2019 Proton Therapy Physics (Medical Physics and Biomedical Engineering) 2nd edn (Boca Raton, Florida: CRC Press)

Parodi K et al. 2007 PET/CT imaging for treatment verification after proton therapy: a study with plastic phantoms and metallic implants Med. Phys 34 419–35 [PubMed: 17388158]

Patch SK et al. 2021 Thermoacoustic range verification during pencil beam delivery of a clinical plan to an abdominal imaging phantom Radiother. Oncol 159 224–30 [PubMed: 33798611]

Pratik Samant L M T, Yong C, Townsend Z and Liangzhong X 2022 3D protoacoustic imaging through a planar ultrasound array: a simulation workflow IEEE Trans. Radiat. Plasma Med. Sci 7 83–95 [PubMed: 37588600]

Schaffner B and Pedroni E 1998 The precision of proton range calculations in proton radiotherapy treatment planning: experimental verification of the relation between CT-HU and proton stopping power Phys. Med. Biol 43 1579–92 [PubMed: 9651027]

Su Z et al. 2019 Impact of intrafraction prostate motion on clinical target coverage in proton therapy: a simulation study of dosimetric differences in two delivery techniques J. Appl. Clin. Med. Phys 20 67–73 [PubMed: 31478341]

Sulak Let al. 1979 Experimental studies of the acoustic signature of proton beams traversing fluid media Nucl. Instrum. Methods 161 203–17

Taasti VT et al. 2018 Comparison of single and dual energy CT for stopping power determination in proton therapy of head and neck cancer Phys. Imaging Radiat. Oncol 6 14–9 [PubMed: 33458383]

Tian L et al. 2021 Accounting for prompt gamma emission and detection for range verification in proton therapy treatment planning Phys. Med. Biol 66 055005 [PubMed: 33171445]

Tryggestad EJ et al. 2020 Managing treatment-related uncertainties in proton beam radiotherapy for gastrointestinal cancers J. Gastrointest. Oncol 11 212–24 [PubMed: 32175124]

Wroska A 2020 Prompt gamma imaging in proton therapy - status, challenges and developments J. Phys. Conf. Ser 1561

Zhang W 2020 Dual-modality x-ray-induced radiation acoustic and ultrasound imaging for real-time monitoring of radiotherapy BME Frontiers 2020 10

Zhu X and El Fakhri G 2013 Proton therapy verification with PET imaging Theranostics. 3 731–40 [PubMed: 24312147]

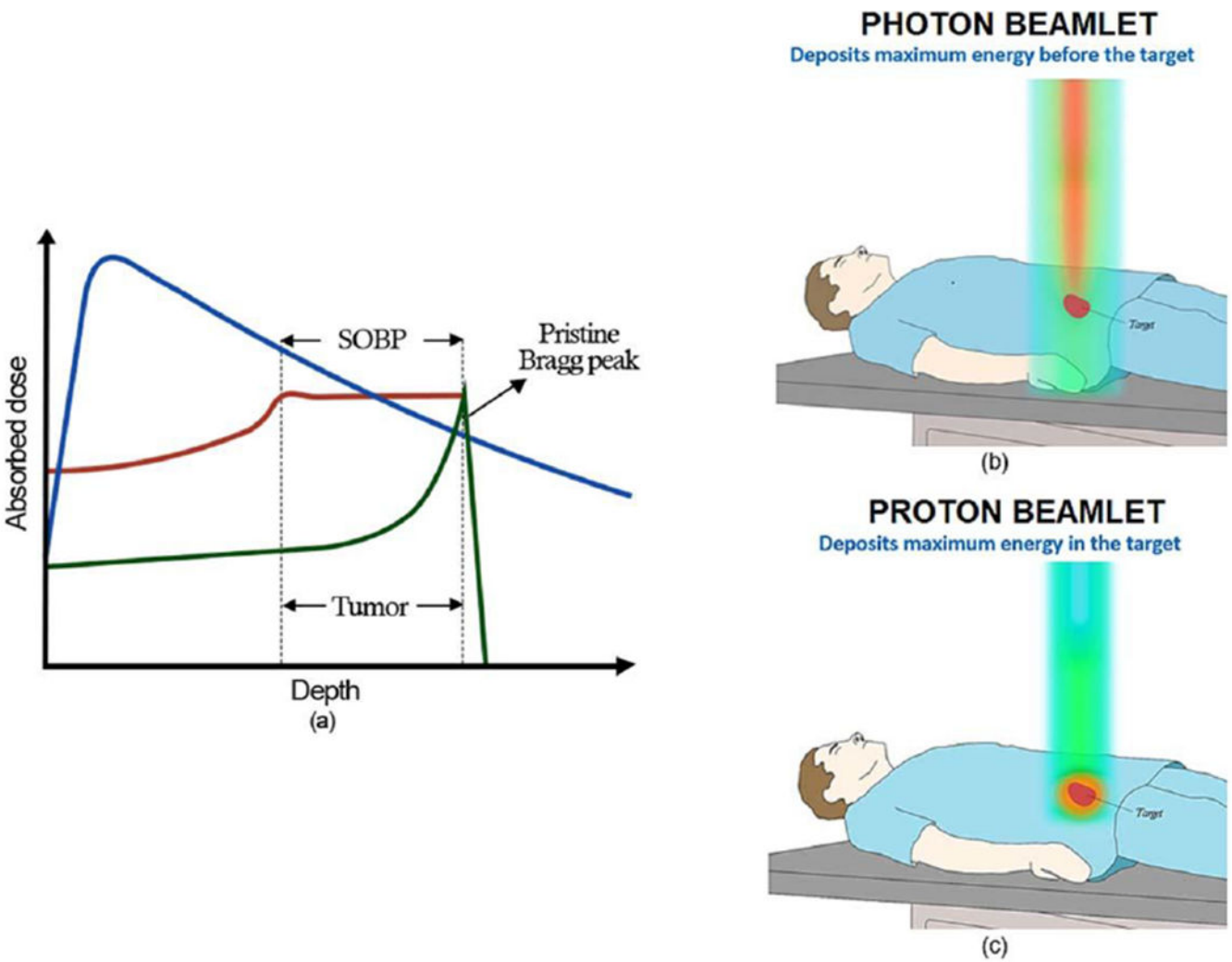

Figure 1.

Proton therapy as the next generation cancer therapy offers dominant advantages over conventional radiation therapy due to the Bragg peak. (a) The comparison of absorbed dose intensity in medium from a single beamlet of photon radiation (blue) to absorbed dose intensity in medium by a proton beamlet, shown with a pristine Bragg peak (green) and a spread-out Bragg peak (SOBP, red). The SOBP is comprised of multiple pristine Bragg peaks that cover the entire tumor depth. (b) The intensity of energy deposition with photon therapy. (c) The intensity of energy deposition with proton therapy.

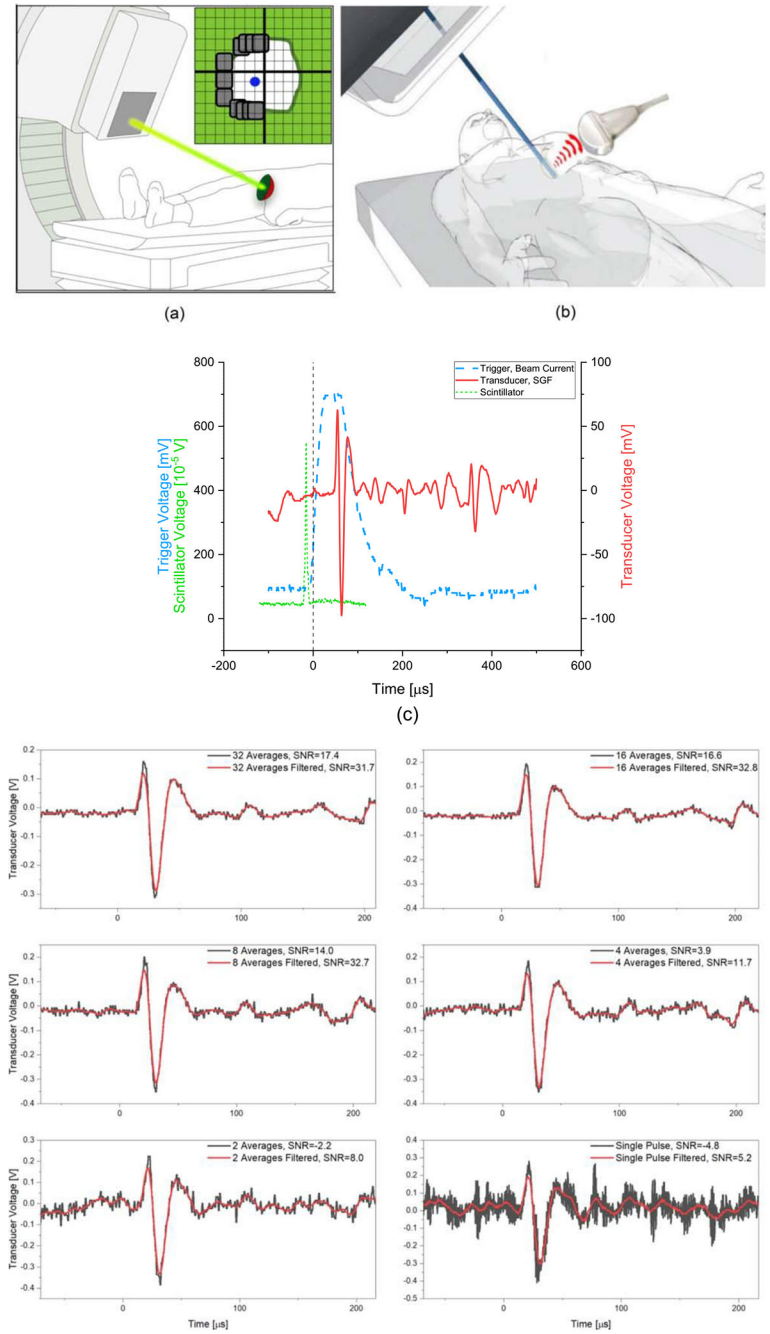

Figure 2.

The feasibility of protoacoustics used as an *in vivo* treatment verification method. (a) The mechanisms of pencil beam scanning with adaptive apertures allow precise and localized spot dose depositions. (b) The physical setup of implementing protoacoustics into clinical treatments. (c) A typical ionoacoustic signal collected by the transducer (1024 avg, 3 pC), with the beam current trigger signal of the proton system. A time delay is associated to the beam current trigger from the scintillator, an ideal trigger. (d) The effect of averaging the signal on the SNR and the importance of digital filtering.

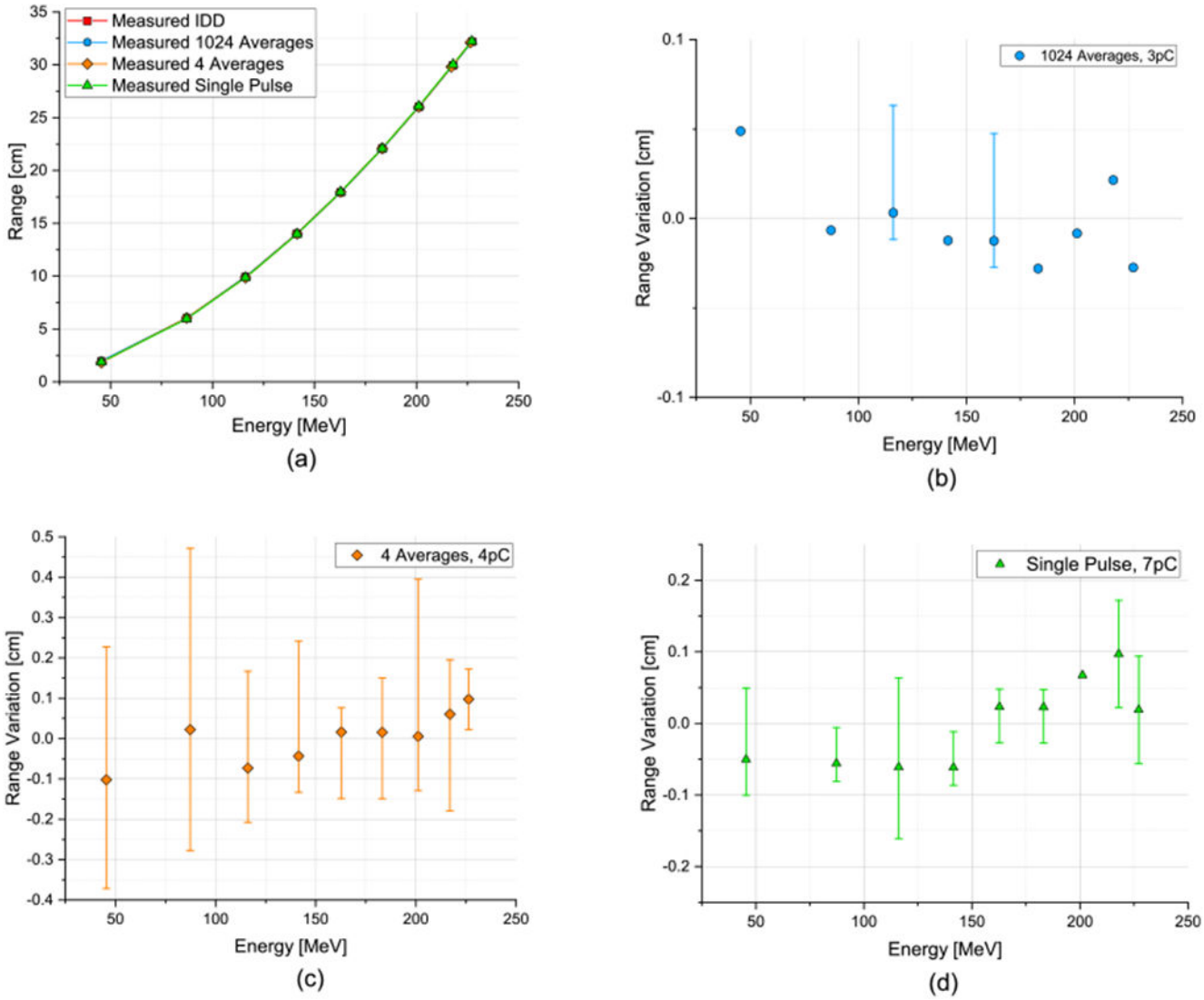

Figure 3.

Protoacoustic range verification results. (a) The energy-range relationship of the proton system. Signals of 1024 averages, 4 averages, and single pulse are compared to the measured ionization depth dose (IDD). (b) The range variations of the 1024 averaged protoacoustic results from the measured IDD curve with a 3 pC/pulse deposition. Displayed error bars correspond to maximum deviations in both directions. (c) The range variations of the 4 averaged protoacoustic results from the measured IDD curve with a 4 pC/pulse deposition. Displayed error bars correspond to maximum deviations in both directions. (d) The range variations of the single pulse protoacoustic results from the measured IDD curve with a 7 pC deposition. Displayed error bars correspond to maximum deviations in both directions.

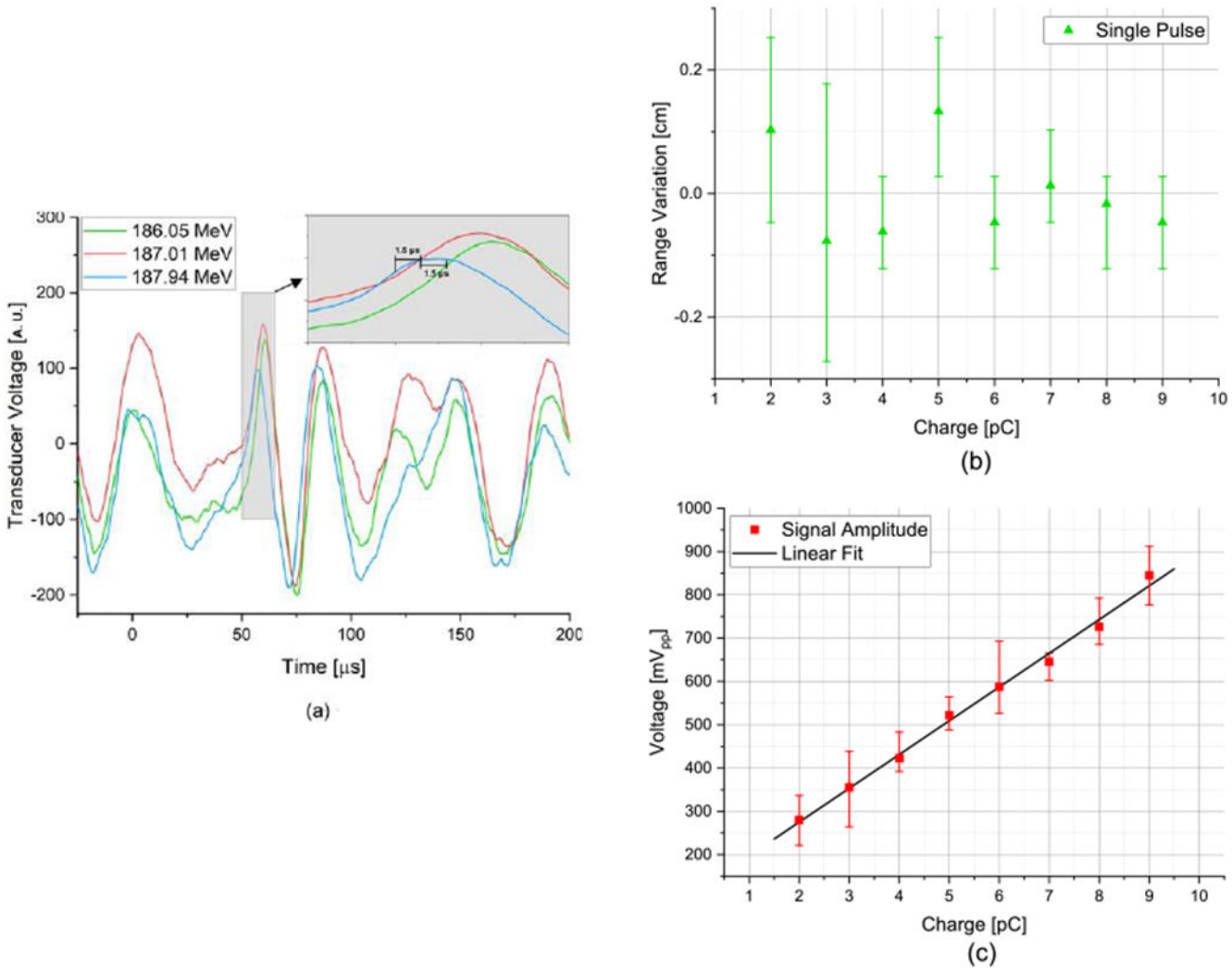

Figure 4.

Protoacoustic resolution and response along beam charge. (a) The resolution of protoacoustic signals (Single pulse, 3 pC) from 2 mm range alterations. The transducer position was set at 35 cm from the entrance window, beam energies of 186.05, 187.01, 187.94 MeV were used. For an approximate distance of 12 cm between Bragg peak and transducer surface. (b) The detected range variations of fixed-energy single pulse protoacoustic signals of various charge depositions from the corresponding IDD. Displayed error bars correspond to maximum deviations in both directions. (c) The linear response of signal voltage from (2–9 pC) charge depositions. Displayed error bars correspond to maximum deviations in both directions. This setup used a transducer position of 28 cm from the entrance window and a beam energy of 162.78 MeV, gradually increasing the charge per pulse. The approximate distance between Bragg peak and transducer surface was 10 cm.

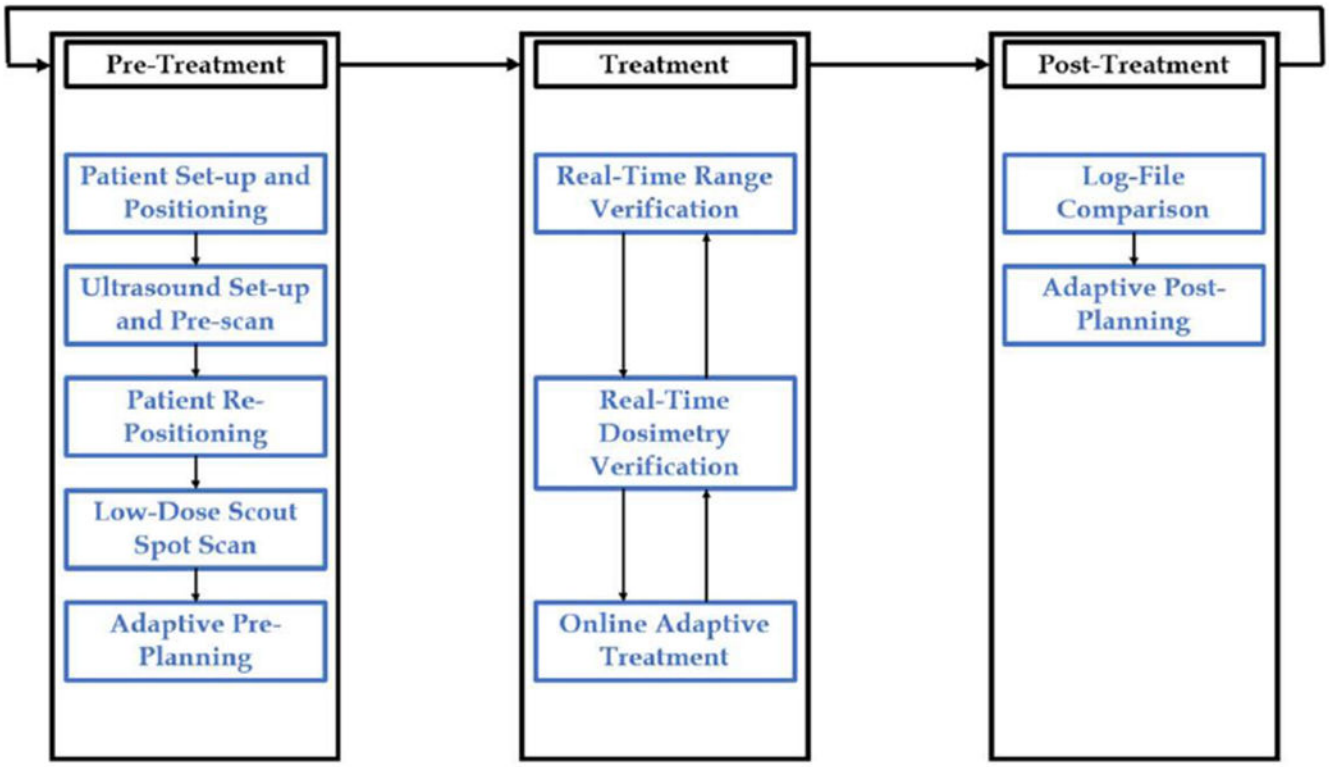

Figure 5.
The future integration of protoacoustics into the clinical workflow.

Table 1.

The percent-maximum of the induced signal at which the correlation point occurs for each beam energy simulated.

Beam energy [MeV]	Percent-maximum
200	0.8407
175	0.6450
150	0.5994
125	0.6112
100	0.6862
75	0.5644
40	0.3713